IEEE Access
Multidisciplinary | Rapid Review | Open Access Journal

Received April 1, 2022, accepted May 19, 2022, date of publication June 13, 2022, date of current version June 22, 2022.

Digital Object Identifier 10.1109/ACCESS.2022.3182696

An Innovate Detumbling Method for a Non-Cooperative Space Target via Repeated Tentative Contacts

DEJIA CHE, ZIXUAN ZHENG, AND JIANPING YUAN
School of Astronautics, Northwestern Polytechnical University, Xi'an 710072, China

Corresponding author: Zixuan Zheng (z.zheng@nwpu.edu.cn)

This work was supported in part by the National Natural Science Foundation of China under Grant 62003269, and in part by the Foundation of Science and Technology on Aerospace Flight Dynamics Laboratory under Grant 6142210200308.

ABSTRACT On-orbit removing tumbling targets is a critical research issue for future space missions. Repeated tentative contacts by the robot can be used to eliminate the rotational motion of a tumbling target. The elimination process depends on the accuracy of the information provided by a motion estimator, which is not discussed in conventional research. Additionally, there are few literatures that examine how to reduce the number of contacts to increase mission safety. To solve these issues, a coupling framework of a navigation method and a detumbling controller is designed in this paper. In particular, the relative navigation method, which incorporates the momentum transfer information and the visual guidance, is developed to estimate states of the target. The combination of two types of information ensures that the estimator can be used continuously in free-floating and contact modes without the need for measuring interaction forces. By modifying an optimal controller, a detumbling controller is designed. A sufficient condition is established such that the robot can achieve the goal of detumbling the target under the influence of estimation errors. Finally, a numerical example is provided to illustrate the effectiveness of the designed framework.

INDEX TERMS Space debris, space robot, state estimation, detumbling controller, repeated contact.

NOMENCLATURE

$\boldsymbol{a}_U$	Vector from the $\{\mathcal{R}\}$ to $\{\mathcal{U}\}$
$\boldsymbol{A}(\cdot)$	Rotation matrix computed by a quaternion
$\boldsymbol{b}$	Robotic knowledge
c_f, c_g, c_ρ	Length of $\boldsymbol{f}_E$, $\boldsymbol{g}$, and $\boldsymbol{\rho}$, respectively
d	Timing of contacts
$\mathcal{D}$	Set of the timing of contacts
$\boldsymbol{f}_E$	Interaction force exerted on the target
$\boldsymbol{f}_R, \boldsymbol{\tau}_R$	Active force/torque generating in the process of orbital/attitude maneuver
$f_{\max}$	Upper threshold of the magnitude of the interaction force
$\boldsymbol{g}$	Angular momentum of the object about the CM
$\boldsymbol{i}_{yz}$	Inertia ratio
$\boldsymbol{I}$	MI of the object described in $\{\mathcal{U}\}$
i_{xx}, i_{yy}, i_{zz}	Principal components of $\boldsymbol{I}$
$\boldsymbol{K}$	Kalman gain matrix
$\boldsymbol{l}, \boldsymbol{p}$	Angular momentum, momentum of the object
$\boldsymbol{l}_R, \boldsymbol{p}_R$	Angular momentum, momentum of the robot
$\boldsymbol{l}_S, \boldsymbol{p}_S$	Angular momentum, momentum of the robot-target system
m	Mass of the object
M	Total number of contacts
N	Dimension of $\boldsymbol{x}$
$\boldsymbol{P}$	Covariance matrix of a variable
$\boldsymbol{Q}$	Covariance matrix of environmental disturbance
$\boldsymbol{q}, \boldsymbol{q}_R$	Quaternion of $\{\mathcal{U}\}$ and $\{\mathcal{R}\}$
$\boldsymbol{q}^*$	Conjugate quaternion of q
$q_s, \boldsymbol{q}_v$	Scalar, vector part of q
$\boldsymbol{q}_{RU}$	Attitude quaternion of $\{\mathcal{U}\}$ relative to $\{\mathcal{R}\}$
$\boldsymbol{r}$	Position of $\{\mathcal{U}\}$ relative to $\{\mathcal{I}\}$
$\boldsymbol{r}_E$	Position of the end-effector relative to $\{\mathcal{I}\}$

The associate editor coordinating the review of this manuscript and approving it for publication was Shih-Hau Fang.

$\boldsymbol{r}_R$	Position of $\{\mathcal{R}\}$ relative to $\{\mathcal{I}\}$
$\boldsymbol{R}$	Covariance matrix of measurement error
$\mathcal{R}$	Set of the position of cloud points
$\boldsymbol{S}$	Cholesky factor of of the error covariance matrix
t_Δ	Sampling time
t_δ	Duration of a contact event
$\boldsymbol{u}$	Angular impulse of a contact about the CM of the object
$u_{\max}$	Maximum magnitude of $\boldsymbol{u}$
$\boldsymbol{v}$	Velocity of the object
$\boldsymbol{v}_R$	Velocity of the robot
w_0^m, w_0^c, w_i^m	Weight parameters of the estimator
$\boldsymbol{w}$	Discrete process noise
$\boldsymbol{x}$	State of the filter
$\mathcal{X}$, $\mathcal{Z}$	Sigma points related to state vector, observation vector
$\boldsymbol{z}$	Observation vector
δ	Dirac delta function
ζ, η, ι, κ	Constant parameters of MCB-SRUKF
$\boldsymbol{\rho}_E$	Vector from $\{\mathcal{U}\}$ to the contact point
$\boldsymbol{\rho}_R$	Vector from $\{\mathcal{U}\}$ to $\{\mathcal{R}\}$
$\boldsymbol{\vartheta}$	Measurement noise
$\boldsymbol{\omega}$	Angular velocities of the object described in $\{\mathcal{U}\}$
$\omega_{\min}$	Allowable residual angular velocity
$\mathbb{R}$, $\mathbb{R}^n$	Set of real numbers or n-dimensional column vectors
$\mathbf{1}_n$	$n \times n$ identity matrix
$\times$	Cross product operation of a vector
$[\cdot\times]$	Cross product matrix
$\otimes$	Quaternion products
$\|\cdot\|$	Euclidean norm
$\cdot^k$	Variable at k-th contact
$\cdot^{\text{unit}}$	Normalized vector of a vector
$\hat{\cdot}$, $\delta\cdot$	Estimated value, error of a variable
$\tilde{\cdot}$	Variables computed by using estimations

ABBREVIATION

CM	Center of mass
EM	Equations of motion
FCDS	Fewest contact detumbling strategy
MC	Momentum conservation
MCB-SQUKF	Momentum-conservation-based square root unscented Kalman filter
MI	Moment of inertia
RCDS	Repeated-contact-detumbling scheme
SASC	Smooth attitude-stabilizing control
SQUKF	Square root unscented Kalman filter

I. INTRODUCTION

Currently, there are a large number of orbital service missions require reliable robotic technology to capture uncooperative objects including dysfunctional satellites and orbital debris [1]. Usually, these targets are tumbling due to the influence of the space environment. The uncertain nature of motion states and inertial parameters is the second uncooperative characteristic. These factors make the capture of uncooperative targets challenging.

Matunaga [2] proposed that the manipulator can absorb the rotational motion of the object by repeatedly contacting with it and applying a slight impulse on it. This method, illustrated in Fig. 1 and named as repeated-contact-detumbling scheme (RCDS) in the following, was a candidate pre-capture approach to reduce the risk of capturing the object. Kawamoto *et al.* [3] proposed that by reducing the nutation and stopping the spinning by turns, a robot can completely dissipate the rotational motion of the object. Yoshikawa and Yamada [4] examined the stationary response under contact model uncertainty and the analytical stability condition of the RCDS. A space target capturing mission carried out by a robot generally consisted of four phases [1]: the pre-capture phase, the impact-contact phase, the post-capture phase, and the compound stabilization phase. In the second phase, RCDS was employed periodically unless the angular velocity of the object was sufficiently small, which ensure that the robot can capture the object safely. Despite the advantage of the RCDS, there exists a few open questions. The detumbling should be performed with the fewest number of contacts possible. However, the optimization problem has not been considered due to the complexity of the RCDS. [2]–[4] indicated that accurate estimations of motion states and inertia parameters of the object are key inputs for the RCDS method. Several navigation methods are discussed in the following to determine whether they can be applied to the RCDS.

Most of estimators for the object removal mission can be classified into three schools according to their primary measurement method: the vision school [5]–[8], the tactile school [9], [10], and the robot-knowledge school [11]–[13]. Some solutions [5], [6] were concerned about free-floating targets and only used vision guidance, which were regarded as the vision school. By incorporating LIDAR sensor data, model-based estimation, and optimal control, Aghili *et al.* developed several autonomous close-range estimation schemes for the space robot [14]–[16]. It is noteworthy that vision-class studies were not able to estimate absolute inertia parameters such as mass and the absolute value of moments of inertia (MI). Shenfield and Rock [17] proposed that all the inertial parameters could be calculated by observing forces and torques exerted on the object. Some researchers, drawing inspiration from them, introduced tactile sensors or force/moment sensors to measure the interaction force/moment between the robotic manipulator and the object. Studies [9], [10] used a Kalman filter to estimate rotational motion in the free-floating mode and a least squares algorithm to determine the MI in the contact mode. A force/moment sensor equipped on the robot is used to collect force and torque information when the robot touches the target. However, extra sensors can lead to a higher cost and power demand. The third school [12], [18], [19] which relies

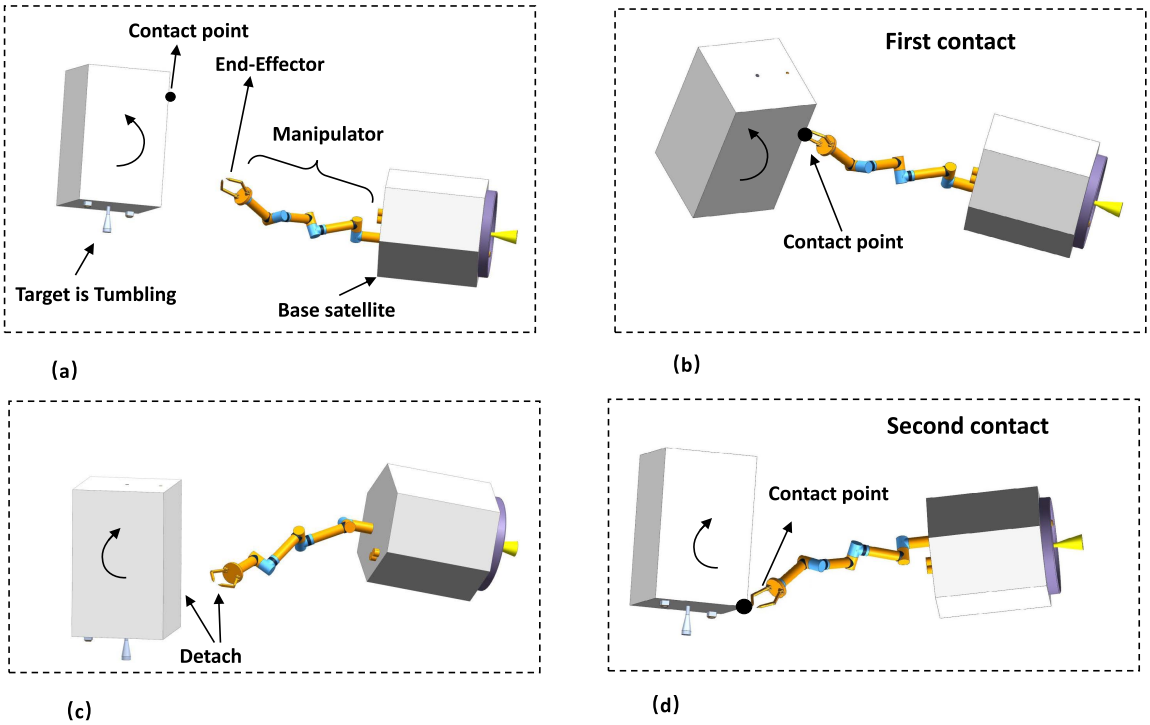

FIGURE 1. The process of RCDS. In (a), the robot tracks the predetermined contact point. The object keeps floating freely. In (b), the controlled collision between the manipulator and the object happens. In (c), the manipulator and the object separate. In (d), a second contact is executed. It should be noted that the robot can choose different contact points according to the motion of the object, as shown in (b) and (d).

on the knowledge of the robot, were widely used in the post-capture phase. Inertial parameters including mass, center of mass (CM), and MI, are calculated by using characteristic parameters and motion states of the robot. However, these algorithms only used motion information of the robot and did not utilize other measurements. Consequently, they were not appropriate for the free-floating motion mode.

Summarizing the aforementioned discussions, we draw several technical problems as follows:

1. The attitude, position, velocity, angular velocity, mass, and MI of the object are unknown. How can a single filter estimates these states under the influence of external disturbance?
2. A series of engineering problems arises from the measuring the interaction force. How can the measurement of the interaction force be avoided in the estimation process?
3. During the RCDS mission, the object can be floating freely or touched by the robot. How can a single filter be designed for this scenario?
4. How to minimize the number of contacts and reduce the risk of RCDS?

To solve all these problems, this paper carries out the research into two parts including constructing an estimator and developing a control algorithm. Main contributions are listed as follows.

1. A novel navigation method, which uses vision guidance and the momentum transfer computation as well as the dynamic model based on the MC law, is developed to estimate inertia parameters and motion information of the object. The only criterion for a usable technique is that it is not affected by the interaction force between the robot and the object.
2. To avoid the oscillation, a detumbling controller is developed by modifying an optimal controller based on Pontryagin's principle. By constructing a Lyapunov function, we demonstrate the stability of the controller in the presence of estimation errors.

A square root unscented Kalman filter (SRUKF) which can maintain the positive semi-definiteness of the high-dimensional covariance matrix [20] is used to construct the estimator. Therefore, the proposed estimator is named as momentum-conservation-based square root unscented Kalman filter or MCB-SRUKF. Combining the detumbling controller with a method of calculating capture points and forces according to the output of the controller is called the Fewest Contact Detumbling Strategy (FCDS). In the RCDS mission as shown in Fig. 2, the object keeps tumbling and floating freely after a contact. The states of the target is estimated by the MCB-SRUKF. The contact point and interaction of the next contact are predetermined by the FCDS to ensure that the detumbling can be alleviated. After that, the space robot predicts and tracks the motion of the contact point by using the estimation of the object. In this paper, we do not discuss the prediction and tracking of a contact point, which were thoroughly examined in [21]–[24]. The contact

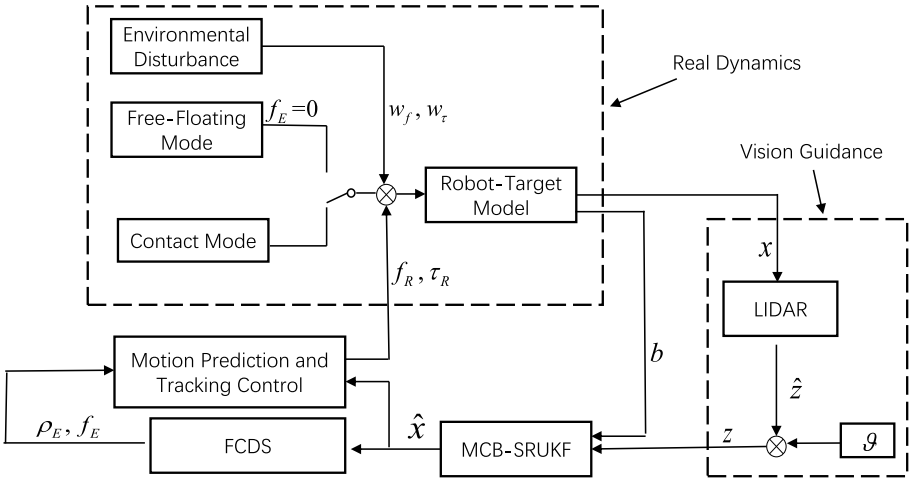

FIGURE 2. The relationship among real dynamics of the RCDS, vision guidance, MCB-SRUKF, FCDS and tracking controller. The object-robot system could be in free-floating mode or the contact mode, as illustrated in the real dynamics box. The environmental disturbing force and torque exerted on the object are considered. Variables are explained in Nomenclature.

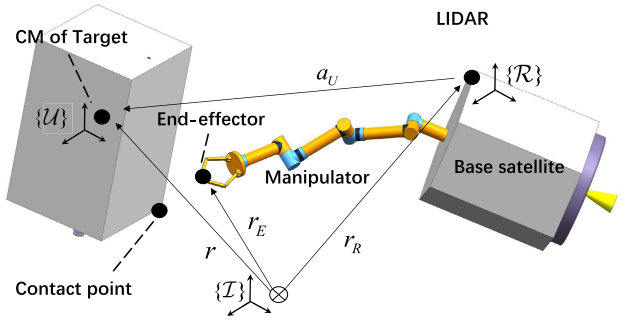

FIGURE 3. The structure of the robot and target.The robot consists of an end-effector, a manipulator, a base satellite, and a LIDAR. The end-effector is controlled to follow the contact point while the target is floating.

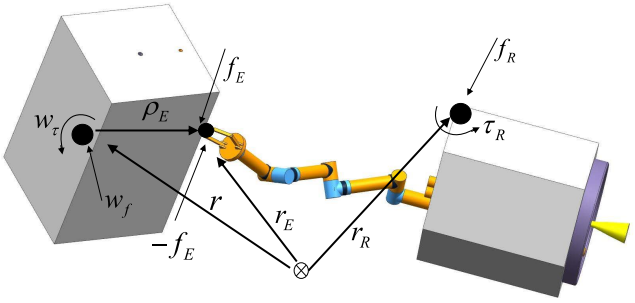

FIGURE 4. Force analysis in the point contact mode. f_E represents the force exerted on the target. The opposite force is exerted on the end-effector. External force/torque on the target are denoted by w_τ and w_f. The active force/torque on the robot are denoted by τ_R and f_R.

detumbling is repetitively executed until the angular velocity of the object becomes enough small.

After this introduction, the MCB-SRUKF are established in Section II. The FCDS is addressed in Section IV. The validation of the coupling scheme of the MCB-SRUKF and FCDS are conducted in Section III. Finally, conclusions are given in Section V.

II. THE DERIVATION OF THE FILTER

A. DYNAMIC ANALYSIS OF THE ROBOT-TARGET SYSTEM

In this section, dynamics of the object and the robot are researched. The structure of the object and the robot are properly simplified, as shown in Fig. 3. The robot coordinate system, denoted as $\{\mathcal{R}\}$, is fixed on the LIDAR. $\{\mathcal{I}\}$ is the inertial frame. The body frame of the object is denoted as $\{\mathcal{U}\}$, which is fixed on the CM. $\{\mathcal{U}\}$ is oriented to the principal axes of MI.

A similar frame system is used for the robot base, denoted as $\{\mathcal{R}\}$. On the left shoulder, the superscript indicates the frame for describing the vector/tensor. The default frame of a vector/tensor is $\{\mathcal{I}\}$, with the exception of $\boldsymbol{\omega}$ and $\boldsymbol{I}$ expressed in $\{\mathcal{U}\}$. Motion states of the robot are presumed to be precisely measured.

Total angular momentum and momentum of the system are as follows:

$$\boldsymbol{l}_S = \boldsymbol{l}_R + \boldsymbol{A}(\boldsymbol{q})\boldsymbol{I}\boldsymbol{\omega} + \boldsymbol{r} \times m\boldsymbol{v} \tag{1}$$

$$\boldsymbol{p}_S = \boldsymbol{p}_R + m\boldsymbol{v} \tag{2}$$

$\boldsymbol{l}_R$ and $\boldsymbol{p}_R$ can be computed by using motion information of the robot which is provided by onboard inertia measurement units and joint encoders, as illustrated in [25], [26]. Therefore, $\boldsymbol{l}_R$ and $\boldsymbol{p}_R$ are considered as inputs to the filter.

The force analysis in the contact mode is shown in Fig. 4. The active force/torque and the interaction force are exerted upon the robot. Active force/torque is generated by the satellite orbit/attitude maneuvering actuator. Therefore, $\boldsymbol{\tau}_R$ and $\boldsymbol{f}_R$ are assumed to be known. Aside from the interaction force, the motion of the object is influenced by others factor, such

as flexible solar panels, fuel sloshing, and gravity gradient. The sum of these three factors are represented by $\boldsymbol{w}$ with the form of $\boldsymbol{w} = \begin{bmatrix} \boldsymbol{w}_\tau^T & \boldsymbol{w}_f^T \end{bmatrix}^T$. Prior research [27] indicates that $\boldsymbol{w}$ can be modeled as zero-mean Gaussian white noise processes with the covariance matrix

$$E\{\boldsymbol{w}_i \boldsymbol{w}_j^T\} = \boldsymbol{Q}\delta_{i,j} \tag{3}$$

For the robot-target system, the change rate of the angular momentum is equal to the resultant moment on the origin of inertia frame, which is

$$\dot{\boldsymbol{l}}_S = \boldsymbol{r}_R \times \boldsymbol{f}_R + \boldsymbol{\tau}_R + \boldsymbol{r} \times \boldsymbol{w}_f + \boldsymbol{w}_\tau \tag{4}$$

The momentum of the system can be calculated by solving the differential equation:

$$\dot{\boldsymbol{p}}_S = \boldsymbol{f}_R + \boldsymbol{w}_f \tag{5}$$

It should be noted that $\boldsymbol{f}_E$ is eliminated in (4) and (5). Two equations also are valid in the free-floating mode as well because $\boldsymbol{f}_E$ is always equal to zero when the object is free-floating. Kinematic equations for the object are the following:

$$\dot{\boldsymbol{q}} = \frac{1}{2}\boldsymbol{\Omega}(\boldsymbol{\omega})\boldsymbol{q} \tag{6}$$

$$\dot{\boldsymbol{r}} = \boldsymbol{v} \tag{7}$$

where $\boldsymbol{\Omega}(\cdot)$ is

$$\boldsymbol{\Omega}(\boldsymbol{\omega}) \equiv \begin{bmatrix} -[\boldsymbol{\omega}\times] & \boldsymbol{\omega} \\ -\boldsymbol{\omega}^T & 0 \end{bmatrix} \tag{8}$$

Dynamics parameters of the object including i_{xx}, m, and $\boldsymbol{i}_{yz}$, are unknown constants and are used as filter states. i_{xx} and $\boldsymbol{i}_{yz}$ are explained in Appendix A. In addition to $\boldsymbol{q}$, $\boldsymbol{r}$, i_{xx}, m, and $\boldsymbol{i}_{yz}$, candidate states include $\boldsymbol{\omega}$, $\boldsymbol{v}$, $\boldsymbol{l}_S$, and $\boldsymbol{p}_S$. According to (1) and (2), $\boldsymbol{l}_S$ and $\boldsymbol{p}_S$ can be computed by $\boldsymbol{\omega}$, $\boldsymbol{v}$, and others states or known variables. Similarly, $\boldsymbol{\omega}$ and $\boldsymbol{v}$ can be solved by rewriting (1) and (2) as

$$\boldsymbol{\omega} = (i_{xx}\boldsymbol{I}_{yz})^{-1}\boldsymbol{A}^T(\boldsymbol{q})(\boldsymbol{l}_S - \boldsymbol{l}_R - \boldsymbol{r} \times (\boldsymbol{p}_S - \boldsymbol{p}_R)) \tag{9}$$

and

$$\boldsymbol{v} = m^{-1}(\boldsymbol{p}_S - \boldsymbol{p}_R) \tag{10}$$

where $\boldsymbol{I}_{yz}$ are explained in Appendix A. Therefore, $\boldsymbol{\omega}$, $\boldsymbol{v}$, $\boldsymbol{l}_S$, and $\boldsymbol{p}_S$ are redundant to the filter. (9) and (10) must be differentiated with respect to time to construct the process equation, if $\boldsymbol{\omega}$ and $\boldsymbol{v}$ are chosen as states of the filter, as in [28]. However, this approach is undesirable because the differentiation of motion states of the robot can introduce errors. (4) and (5) can be used as process equations of the filter if $\boldsymbol{l}_S$ and $\boldsymbol{p}_S$ are considered as states. The second method reduces computing complexity and can prevent truncation errors. Therefore, $\boldsymbol{\omega}$ and $\boldsymbol{v}$ are considered intermediate variables that can be computed by using $\boldsymbol{p}_S$, $\boldsymbol{l}_S$, and other variables.

States of the filter can be summarized as follows:

$$\boldsymbol{x} = \begin{bmatrix} \boldsymbol{q}^T & \boldsymbol{r}^T & \boldsymbol{l}_S^T & \boldsymbol{p}_S^T & i_{xx} & m & \boldsymbol{i}_{yz}^T \end{bmatrix}^T \tag{11}$$

Robotic knowledge used in (4), (5), (9), and (10) is written as a single vector which is

$$\boldsymbol{b} = \begin{bmatrix} \boldsymbol{l}_R^T & \boldsymbol{p}_R^T & \boldsymbol{r}_R^T & \boldsymbol{q}_R^T & \boldsymbol{\tau}_R^T & \boldsymbol{f}_R^T \end{bmatrix}^T \tag{12}$$

In this section, the dynamic of the system is presented in the form of (4), (5), (6), (7), (9), and (10). Momentum transfer is used as an indirect measurement of the velocity/angular velocity. Taking the prediction of the velocity and the position of the object as an example: The total momentum is predicted according to Eq. (5); The momentum and velocity of the object are calculated by subtracting the robot momentum from the total momentum, as shown in (10); The object position is calculated after solving differential equation of (7). The angular momentum, the velocity and the attitude of the object can be calculated in the same way. The indirect method has several advantages over the traditional acceleration formulas which are widely used in previous studies [29], [30]. The proposed method is not affected by the interaction force and is appropriate for two motion modes. The method does not require any additional sensors.

B. PROCESS EQUATIONS AND OBSERVATION EQUATIONS

In this subsection, dynamic equations mentioned above are transformed into discrete process equations. (4), (5), (6), and (7) are integrated and discretized. $\boldsymbol{x}_k$ is propagated forward by

$$\boldsymbol{q}_k = \boldsymbol{\Theta}(\boldsymbol{\omega}_{k-1})\boldsymbol{q}_{k-1} \tag{13}$$

$$\boldsymbol{r}_k = \boldsymbol{v}_{k-1}t_\Delta + \boldsymbol{r}_{k-1} \tag{14}$$

$$\begin{aligned} \boldsymbol{l}_{S,k} = \boldsymbol{l}_{S,k-1} + t_\Delta(&\boldsymbol{r}_{R,k-1} \times \boldsymbol{f}_{R,k-1} + \tau_{R,k-1} \\ &+ \boldsymbol{r}_{k-1} \times \boldsymbol{w}_{f,k-1} + \boldsymbol{w}_{\tau,k-1}) \end{aligned} \tag{15}$$

$$\boldsymbol{p}_{S,k} = \boldsymbol{p}_{S,k-1} + t_\Delta(\boldsymbol{f}_{R,k-1} + \boldsymbol{w}_{f,k-1}) \tag{16}$$

$$i_{xx,k} = i_{xx,k-1} \tag{17}$$

$$m_k = m_{k-1} \tag{18}$$

$$\boldsymbol{i}_{yz,k} = \boldsymbol{i}_{yz,k-1} \tag{19}$$

where $\boldsymbol{\omega}_{k-1}$ and $\boldsymbol{v}_{k-1}$ are calculated by substituting $\hat{\boldsymbol{x}}_{k-1}$ into (9) and (10). $\boldsymbol{\Theta}$ in (13) can be derived by (6). It has the form of

$$\boldsymbol{\Theta}(\boldsymbol{\omega}) \equiv cos(t_\Delta \|\boldsymbol{\omega}\|/2)\boldsymbol{1}_4 + \begin{bmatrix} -[\boldsymbol{\psi}\times] & \boldsymbol{\psi} \\ -\boldsymbol{\psi}^T & 0 \end{bmatrix} \tag{20}$$

where $\boldsymbol{\psi} \equiv sin(t_\Delta \|\boldsymbol{\omega}\|/2)\boldsymbol{\omega}/\|\boldsymbol{\omega}\|$. Discrete process equations can be compiled into a compact form

$$\boldsymbol{x}_k = \boldsymbol{f}(\boldsymbol{x}_{k-1}, \boldsymbol{b}_{k-1}) + \boldsymbol{G}(\boldsymbol{x}_{k-1})\boldsymbol{w}_{k-1} \tag{21}$$

where $\boldsymbol{G}(\boldsymbol{x}_{k-1})$ is

$$\boldsymbol{G}(\boldsymbol{x}_{k-1}) = t_\Delta \begin{bmatrix} \boldsymbol{0}_{7\times3} & \boldsymbol{0}_{7\times3} \\ \boldsymbol{1}_3 & [\boldsymbol{r}_{k-1}\times] \\ \boldsymbol{0}_{3\times3} & \boldsymbol{1}_3 \\ \boldsymbol{0}_{4\times3} & \boldsymbol{0}_{4\times3} \end{bmatrix} \tag{22}$$

Observation equations are then investigated. The orientation and position of $\{\mathcal{U}\}$ relative to the robot frame $\{\mathcal{R}\}$ can be calculated by range data of the point cloud provided by

the LIDAR according to [6], [10]. Considering the measuring error of the LIDAR which is denoted by $\boldsymbol{\vartheta}$, the measurement vector is

$$z_k = \begin{bmatrix} {}^R\boldsymbol{a}_U \\ \boldsymbol{q}_{RU} \end{bmatrix} + \boldsymbol{\vartheta}_k \tag{23}$$

where ${}^R\boldsymbol{a}_U$ represents $\boldsymbol{a}_U$ described in $\{\mathcal{R}\}$. Using experimental data from a previous study [21], the measurement error of LIDAR can be modeled as known Gaussian white-noise processes. Therefore, means and covariances of $\boldsymbol{\vartheta}_k$ can be written as

$$E\{\boldsymbol{\vartheta}_i\} = 0 \tag{24}$$

$$E\{\boldsymbol{\vartheta}_i \boldsymbol{\vartheta}_j^T\} = \boldsymbol{R}\delta_{i,j} \tag{25}$$

In Fig. 3, the position and the orientation of the target relative to the robot, denoted by ${}^R\boldsymbol{a}_U$ and $\boldsymbol{q}_{RU}$, are measured by the LIDAR. According to the figure, $\boldsymbol{a}_U$ can be computed by

$$\boldsymbol{a}_U = \boldsymbol{r} - \boldsymbol{r}_R \tag{26}$$

${}^R\boldsymbol{a}_U$ is the value of $\boldsymbol{a}_U$ described in $\{\mathcal{R}\}$ and can be calculated by

$${}^R\boldsymbol{a}_U = \boldsymbol{A}^T(\boldsymbol{q}_R)(\boldsymbol{r} - \boldsymbol{r}_R) \tag{27}$$

$\boldsymbol{q}$ and $\boldsymbol{q}_R$ are orientations of $\{\mathcal{U}\}$ and $\{\mathcal{R}\}$, respectively. According to the quaternion operation, the quaternion of $\{\mathcal{U}\}$ relative to $\{\mathcal{R}\}$ is

$$\boldsymbol{q}_{RU} = \boldsymbol{q} \otimes \boldsymbol{q}_R^* \tag{28}$$

where $\boldsymbol{q}\otimes$ represents $\boldsymbol{q}\otimes \equiv q_s\mathbf{1}_4 + \boldsymbol{\Omega}(\boldsymbol{q}_v)$. $\boldsymbol{q}^*$ is given by $\boldsymbol{q}^* \equiv \begin{bmatrix} -\boldsymbol{q}_v^T & q_s \end{bmatrix}^T$. All variables on the right hand side of (27) and (28) are included in $\boldsymbol{u}$ and $\boldsymbol{x}$. Therefore, (27) and (28) can be written as

$$\begin{bmatrix} {}^R\boldsymbol{a}_U \\ \boldsymbol{q}_{RU} \end{bmatrix} = \boldsymbol{h}(\boldsymbol{x}, \boldsymbol{u}) \tag{29}$$

Substituting (29) into (23), the measurement of the vision guidance is

$$z_k = \boldsymbol{h}(\boldsymbol{x_k}, \boldsymbol{b_{k-1}}) + \boldsymbol{\vartheta}_k \tag{30}$$

In this section, process equations and measuring equations are built. A series of Kalman filter can be used to construct the estimator. A square root unscented Kalman filter (SRUKF) which is reviewed in Appendix B is used in this paper due to the computational stability.

C. SUPPLEMENTARY INSTRUCTION OF THE FILTER

The natural law that m, i_{xx}, $\boldsymbol{l}_S$, and $\boldsymbol{p}_S$ cannot be estimated before the first contact occurs is followed by the MCB-SRUKF. The estimation of $\boldsymbol{q}$, $\boldsymbol{r}$, $\boldsymbol{\omega}$, $\boldsymbol{v}$, $\boldsymbol{i}_{yz}$ is not affected by this phenomenon, denoted by the semi-activation. Activating the filter requires that the interaction force is not equal to zero, and $\boldsymbol{f}_E$ cannot be parallel to $\boldsymbol{\rho}_E$. These conditions can be summed up as $\boldsymbol{\rho}_E \times \boldsymbol{f}_E \neq 0$.

This condition requires reasonable settings, especially the contact point and the interaction force. The FCDS which automatically meets the demand of $\boldsymbol{\rho} \times \boldsymbol{f}_E \neq 0$, is presented in the next section. By using the FCDS and MCB-SRUKF, two purposes can be achieved after several contacts: estimating all states including m, i_{xx}, $\boldsymbol{l}_S$, and $\boldsymbol{p}_S$; and detumbling the object with the least of number of contacts.

III. FEWEST CONTACT DETUMBLING STRATEGY

The construction of the FCDS takes three steps. Firstly, the attitude dynamic of the object is investigated along with the effect of estimation errors on the angular momentum about the CM of the object. Secondly, a sub-optimal controller is designed. The stability proof of the controller is given under the existence of estimation errors. Thirdly, the method for determining the contact point and interaction force by using the control quantity is developed.

A. PROBLEM STATEMENT AND ERROR ANALYSIS IN THE DETUMBLING TASK

The attitude of the object is influenced by the interaction force and disturbance torque as discussed in Section II-A. The interaction force is not equal to zero at contacts. This can be expressed as that $\boldsymbol{f}_{E,k} \neq 0$ when $k \in \mathcal{D}\left\{d^1, \ldots, d^i, \ldots, d^M\right\}$ where d^i represents the time of i-th contact and M is the total number of contacts. During the free mode, the influence of disturbance torque on the attitude can be estimated by the filter. It is reasonable to ignore the environmental disturbance in this section. Therefore, the angular momentum about the CM of the object, denoted by $\boldsymbol{g}$, changes only at contacts and is a constant vector between two contacts, which is stated as:

$$\boldsymbol{g}^{i,-} = \boldsymbol{g}^{i-1,+} \tag{31}$$

where $\boldsymbol{g}^{i,-}$ and $\boldsymbol{g}^{i-1,+}$ represent the $\boldsymbol{g}$ right before d^i and right after d^{i-1}. The relationship between $g^{i,+}$ and $g^{i,-}$ can be written as

$$\boldsymbol{g}^{i,+} = \boldsymbol{g}^{i,-} + t_\delta \boldsymbol{\rho}_E^i \times \boldsymbol{f}_E^i \tag{32}$$

where t_δ is the duration of a contact. Assuming that the length of $\boldsymbol{\rho}_E^i$ is constant, denoted by c_ρ. For safety, the magnitude of the contact force cannot exceed a certain value which is denoted by f_{max}. The second term in the right side of (32) is regarded as the control variable, denoted as $\boldsymbol{u}$. For simplicity, the plus superscript of $\boldsymbol{g}^{i,+}$ is omitted. Combining (31), (32) can be rewritten as

$$\boldsymbol{g}^i = \boldsymbol{g}^{i-1} + \boldsymbol{u}^i \tag{33}$$

The physical meanings of $\boldsymbol{u}^i$ is the angular impulse about the CM of the object at the i-th contact. $\boldsymbol{g}$ can be calculated by states of the estimator:

$$\boldsymbol{g} = \boldsymbol{A}\boldsymbol{I}\boldsymbol{\omega} = i_{xx}\boldsymbol{A}(q)\,\boldsymbol{I}_{yz}\boldsymbol{\omega} \tag{34}$$

The length and unit vector of $\boldsymbol{g}$ are denoted by c_g and $\boldsymbol{g}^{\text{unit}}$. Considering that $\boldsymbol{A}^T\boldsymbol{A} = \mathbf{1}_3$, they have the form of

$$c_g = i_{xx} \left\| \boldsymbol{I}_{yz}\boldsymbol{\omega} \right\| \tag{35}$$

and

$$\boldsymbol{g}^{\text{unit}} = \boldsymbol{A}(q)\boldsymbol{I}_{yz}\boldsymbol{\omega} / \left\|\boldsymbol{I}_{yz}\boldsymbol{\omega}\right\| \tag{36}$$

Assuming that the controller can be designed to be $\boldsymbol{u}^i = \boldsymbol{u}^i(\tilde{\boldsymbol{g}}^{i-1}, d^i)$, where $\tilde{\boldsymbol{g}}$ is computed by $\hat{\boldsymbol{x}}$. Assuming that the relationship between $\boldsymbol{g}$ and $\tilde{\boldsymbol{g}}$ has the form of

$$\tilde{\boldsymbol{g}} = a_g \boldsymbol{g} + \boldsymbol{\epsilon}_g \tag{37}$$

where $\boldsymbol{g} \cdot \boldsymbol{\epsilon}_g = 0$. The relatively precise estimation of $\boldsymbol{q}$, $\boldsymbol{I}_{yz}$, and $\boldsymbol{\omega}$ in (36) always can be provided by the filter. Therefore, the angle between $\boldsymbol{g}$ and $\tilde{\boldsymbol{g}}$ is small. We can solve a_g and $\boldsymbol{\epsilon}_g$ with the form of

$$a_g = \frac{\tilde{c}_g}{c_g} = \frac{\hat{i}_{xx}}{i_{xx}} \cdot \frac{\left\|\hat{\boldsymbol{I}}_{yz}\hat{\boldsymbol{\omega}}\right\|}{\left\|\boldsymbol{I}_{yz}\boldsymbol{\omega}\right\|} \tag{38}$$

and

$$\boldsymbol{\epsilon}_g = \tilde{c}_g(\tilde{\boldsymbol{g}}^{\text{unit}} - \boldsymbol{g}^{\text{unit}}) \tag{39}$$

$\tilde{\boldsymbol{g}}$ and $\boldsymbol{g}$ have same magnitude when $a_g = 1$. $\tilde{\boldsymbol{g}}$ is parallel to $\boldsymbol{g}$ if $\boldsymbol{\epsilon}_g = \boldsymbol{0}$. Before the first contact, there is much difference between a_g and 1 because the semi-activated filter cannot estimated i_{xx}. Considering that $\boldsymbol{\epsilon}_g$ is far smaller than $\boldsymbol{g}$, we assume that there exists a common maximum magnitude of $\boldsymbol{\epsilon}_g$, denoted by $\epsilon_{\max}$.

B. DESIGN AND STABILITY ANALYSIS OF THE CONTROLLER

According to (33) and (37), the attitude dynamic of the object is as follows:

$$\boldsymbol{g}^i = \boldsymbol{g}^{i-1} + \boldsymbol{u}^i(\tilde{\boldsymbol{g}}^{i-1}, d^i), \quad i \in [1, \ldots, M] \tag{40}$$

where

$$\tilde{\boldsymbol{g}}^{i-1} = a_g^{i-1}\boldsymbol{g}^{i-1} + \boldsymbol{\epsilon}_g^{i-1}, \quad i \in [1, \ldots, M] \tag{41}$$

subject to

$$\left\|\boldsymbol{u}^i\right\| \le u_{\max} = t_\delta c_\rho f_{\max} \tag{42}$$

$$a_g^{i-1} > 0 \tag{43}$$

and

$$\left\|\boldsymbol{\epsilon}_g^{i-1}\right\| \le \epsilon_{\max} \tag{44}$$

Boundary conditions are

$$\boldsymbol{g}^0 = \boldsymbol{g}(0) \tag{45}$$

and

$$\boldsymbol{g}^M = 0 \tag{46}$$

It should be noted that the time interval of the discrete controller is equal to the time it takes between two contacts, which is longer than the time interval of the system mentioned in Section II-B. The controller is designed to make $\boldsymbol{\omega}$ or $\boldsymbol{l}_C$ equal to zero with the fewest number of contacts. Therefore, the cost function of the control problem can be formulated as

$$J = F_1(\boldsymbol{g}^M, M) + \sum_{i=0}^{M-1} F_2(\boldsymbol{g}^i, \boldsymbol{u}^i, i) \tag{47}$$

Based on Pontryagin's maximum principle, a discrete optimal controller is derived in Appendix C. It has the form of

$$\boldsymbol{u}^i = -u_{\max}\frac{\boldsymbol{g}^0}{\left\|\boldsymbol{g}^0\right\|} \tag{48}$$

This is not a feedback control and is not robust to any disturbance. The optimal continuous detumbling controller developed by Farhad [31] is the equivalent of

$$\boldsymbol{u}^i = -u_{\max}\frac{\boldsymbol{g}^{i-1}}{\left\|\boldsymbol{g}^{i-1}\right\|} \tag{49}$$

It cannot guarantee the convergence of $\boldsymbol{g}$ in the discrete system and can lead to the chattering if $\|\boldsymbol{g}\| \le u_{\max}$. We have to develop a novel controller which is robust against measurement errors. Two controllers reveals that an optimal detumbling controller must keeps the direction of $\boldsymbol{u}$ opposite to $\boldsymbol{g}$. Therefore, a sub-optimal proportional controller is given:

$$\boldsymbol{u}^i = -u_{\max}\text{Tanh}\left(\frac{\left\|\tilde{\boldsymbol{g}}^{i-1}\right\|}{u_{\max}}\right)\frac{\tilde{\boldsymbol{g}}^{i-1}}{\left\|\tilde{\boldsymbol{g}}^{i-1}\right\|} \tag{50}$$

A hyperbolic tangent coefficient is used to make $\boldsymbol{u}^i \doteq -\tilde{\boldsymbol{g}}^{i-1}$ when $\left\|\tilde{\boldsymbol{g}}^{i-1}\right\| < u_{\max}$. Therefore, the residual rotational motion can be eliminated without the chattering.

To validate the stability of the controller, a Lyapunov function is considered:

$$V = \boldsymbol{g}^T\boldsymbol{g}/2 \tag{51}$$

Combining (40) and (50), the differentiation of V with respect to time can be computed as

$$\begin{aligned}
&\left.\frac{\Delta V}{\Delta t}\right|_{k=d^{i-1}} \\
&= \boldsymbol{g}^{i-1,T}\boldsymbol{u}^i \\
&= -\boldsymbol{g}^{i-1,T}u_{\max}\text{Tanh}\left(\frac{\left\|\tilde{\boldsymbol{g}}^{i-1}\right\|}{u_{\max}}\right)\frac{a_g^{i-1}\boldsymbol{g}^{i-1} + \boldsymbol{\epsilon}_g^{i-1}}{\left\|\tilde{\boldsymbol{g}}^{i-1}\right\|} \\
&\le -\frac{u_{\max}}{\left\|\tilde{\boldsymbol{g}}^{i-1}\right\|}\text{Tanh}\left(\frac{\left\|\tilde{\boldsymbol{g}}^{i-1}\right\|}{u_{\max}}\right)(a_g^{i-1}\left\|\boldsymbol{g}^{i-1}\right\|^2 \\
&\quad -\epsilon_{\max}\left\|\boldsymbol{g}^{i-1}\right\|)
\end{aligned} \tag{52}$$

Considering that $a_g^{i-1} > 0$, we can find that

$$\frac{\Delta V}{\Delta t} \le 0 \tag{53}$$

when

$$\left\|\boldsymbol{g}^{i-1}\right\| \ge \epsilon_{\max}/a_g^{i-1} \tag{54}$$

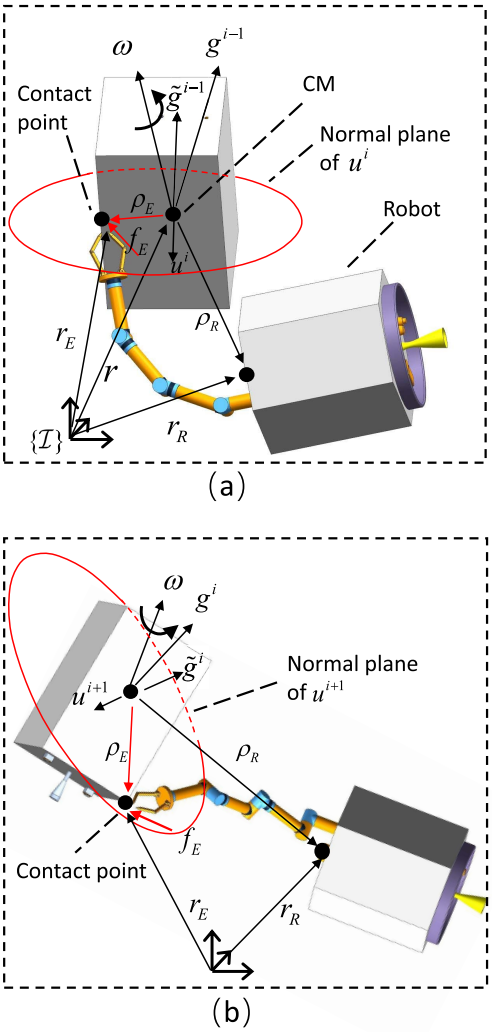

FIGURE 5. The detumbling of the object executed by the robot. (a) and (b) represent scenes at the moments of $k = d^{i-1}$ and $k = d^i$, respectively. Vectors which are marked as red arrows lie on the normal plane of u (red curve). It should be noted that contact points and contact forces in two subgraphs are different.

is satisfied. Therefore, we can conclude that $\boldsymbol{g}$ can always converge into the region of $\|\boldsymbol{g}^{i-1}\| < \epsilon_{\max}/a_g^{i-1}$. The semi-activated filter does not affect the convergence trend although it makes a_g deviate from 1. On the other hand, $\boldsymbol{g}$ cannot completely equal zero in the presence of $\boldsymbol{\epsilon}_g$. Therefore, the residual rotation of the object is inevitable due to the inexact estimation.

C. REALIZATION OF THE CONTROLLER

Optimal contact points and interaction forces are determined in this subsection to generate the desired output contact. $\boldsymbol{\rho_E}$ and $\boldsymbol{f_E}$ lie on the normal plane of $\boldsymbol{u}$ as shown in Fig. 5 due to

$$\boldsymbol{u} = t_\delta \boldsymbol{\rho}_E \times \boldsymbol{f}_E \tag{55}$$

TABLE 1. Inertial parameters of the robot and those of the object.

	Mass, kg	i_{xx}, kg · m^2	i_{yy}, kg · m^2	i_{zz}, kg · m^2
Robot base	2550	6200	3540	7090
Link 1	35.0	0.25	0.25	1.69
Link 2	22.5	0.10	1.31	3.75
Link 3	21.9	0.10	0.71	2.53
Link 4	16.5	0.15	0.15	0.073
Link 5	26.0	0.15	0.15	0.13
Link 6	18.5	0.97	0.97	0.26
Target	1200	1600	900	1800

An unit vector of $\boldsymbol{\rho}_E$ which is perpendicular to $\boldsymbol{u}$ can be computed by

$$\boldsymbol{\rho}_E^{\text{unit}} = \frac{\boldsymbol{u} \times \boldsymbol{\rho_R}}{\|\boldsymbol{u} \times \boldsymbol{\rho_R}\|} \tag{56}$$

where $\boldsymbol{\rho_R}$ is

$$\boldsymbol{\rho_R} = \boldsymbol{r_R} - \hat{\boldsymbol{r}} \tag{57}$$

$\boldsymbol{\rho_R}$ can be replaced by other applicable vectors. The position dataset of 3-D point clouds provided by the vision guidance is given as $\mathcal{R} = \{\hat{\boldsymbol{r}}_1^{\text{cloud}} \ldots \hat{\boldsymbol{r}}_m^{\text{cloud}}\}$. The vector from the CM to the j-th cloud point is parallel to $\boldsymbol{\rho}_E^{\text{unit}}$ if

$$(\hat{\boldsymbol{r}}_j^{\text{cloud}} - \hat{\boldsymbol{r}}) \times \boldsymbol{\rho}_E^{\text{unit}} = 0 \tag{58}$$

is met. The j-th point is selected as the contact point. $\boldsymbol{\rho_E}$ can be rewritten as

$$\boldsymbol{\rho_E} = \hat{\boldsymbol{r}}_i^{\text{cloud}} - \hat{\boldsymbol{r}} = c_\rho \boldsymbol{\rho}_E^{\text{unit}} \tag{59}$$

To generalize maximal torque, the active force are perpendicular to $\boldsymbol{\rho_E}$. Accordingly, the active force can be determined by

$$\boldsymbol{f_E} = c_f \frac{\boldsymbol{u} \times \boldsymbol{\rho_E}}{\|\boldsymbol{u} \times \boldsymbol{\rho_E}\|} \tag{60}$$

where c_f is the length of $\boldsymbol{f_E}$. Substituting (50), (56), (59), and (60) into (55), c_f can be solved by

$$c_f = \frac{u_{\max}}{t_\delta c_\rho} \text{Tanh}\left(\frac{\|\tilde{\boldsymbol{g}}\|}{u_{\max}}\right) \tag{61}$$

Therefore, the contact points and interaction forces which are used to generate expected $\boldsymbol{u}$ are determined.

In the FCDS, the control is carried out by selecting sub-optimal contact points and interaction forces until the magnitude of the angular velocity of the object does not exceed a predefined value, denoted by $\omega_{\min}$. Therefore, the MCB-SRUKF and FCDS can be summarized as pseudo-code (Algorithm 1).

IV. SIMULATION

A. SIMULATION SCHEME

In this paper, to simulate the real robot-target environment, we employ the famous ETS-VII mission as the background. The manipulator of the ETS-VII is composed of six rigid links. The end-effector can be seen as a part of the sixth link. Detailed related inertia parameters of the robot base, manipulator links, and the target are shown in Table 1. Initial motion parameters of the robot-target system are presented in Table 2. SpaceDyn [32], a space robot simulation toolbox for

Algorithm 1

Input: initial guess of the state vector $\hat{\boldsymbol{x}}_0$, initial guess of the covariance $\hat{\boldsymbol{S}}_0$, maximum discrete time $k_{\max}$, contact timing set $\mathcal{D}$, magnitude of allowed residual angular velocity $\omega_{\min}$, magnitude of maximum allowed interaction force $f_{\max}$, mean radius of the object c_ρ, duration of a contact t_δ

Output: estimation set $\boldsymbol{X}$, contact point set $\boldsymbol{C}_\rho$, contact force set $\boldsymbol{C}_f$

for $k = 1 : k_{\max}$ **do**
  z_k and $\boldsymbol{b_k}$ are calculated or measured.
  $\hat{\boldsymbol{x}}_k, \hat{\boldsymbol{S}}_k \leftarrow \hat{\boldsymbol{x}}_{k-1}, \hat{\boldsymbol{S}}_{k-1}, z_k$, and $\boldsymbol{b_k}$ according to (74)-(86).
  if $k \in \mathcal{D}$ && $\left\|\hat{\boldsymbol{\omega}}\right\| > \omega_{\min}$ **then**
    $\mathcal{R}$ is called from the range image generated by LIDAR.
    $\tilde{\boldsymbol{g}} \leftarrow \hat{\boldsymbol{x}_k}$ according to (34).
    $u_{\max} \leftarrow f_{\max}$, c_ρ, and t_δ according to (42).
    $\boldsymbol{u} \leftarrow u_{\max}, \tilde{\boldsymbol{g}}$ according to (50).
    $\boldsymbol{\rho_E} \leftarrow \hat{\boldsymbol{x}_k}$, $\boldsymbol{r_{R,k}}$, $\boldsymbol{u}$, and $\mathcal{R}$ according to (56), (57), (58), and (59)
    $\boldsymbol{f_E} \leftarrow \boldsymbol{\rho_E}, \tilde{\boldsymbol{g}}, \boldsymbol{u}, u_{\max}, t_\delta$, and c_ρ according to (60) and (61).
  else
    break
  end if
  $\hat{\boldsymbol{x}}_{k-1} \leftarrow \hat{\boldsymbol{x}}_k, \hat{\boldsymbol{S}}_{k-1} \leftarrow \hat{\boldsymbol{S}}_k$
end for

return $\boldsymbol{X} = \{\hat{\boldsymbol{x}}_1, \ldots, \hat{\boldsymbol{x}}_{k_{\max}}\}$, $\boldsymbol{C}_\rho = \{\boldsymbol{\rho}_E^1, \ldots, \boldsymbol{\rho}_E^M\}$, $\boldsymbol{C}_f = \{\boldsymbol{f}_E^1, \ldots, \boldsymbol{f}_E^M\}$

MATLAB with high computational efficiency, is used in this paper.

Precision parameters of LIDAR are reported in [21]. The measuring frequency of the LIDAR is set as 2.5Hz. The covariance matrix of the measurement noise is $\boldsymbol{R} = \text{diag}(0.045^2 \times \mathbf{1}_3 \text{m}^2, 0.06^2 \times \mathbf{1}_4)$. t_δ and c_ρ are set to 1s and 3m, respectively. The covariance matrix of environmental disturbances is $\boldsymbol{Q} = \text{diag}(1.8^2 \times \mathbf{1}_3 kg^2 \cdot \text{m}^4/s^4, 1.2^2 \times \mathbf{1}_3 kg^2 \cdot \text{m}^2/s^4)$. The robot is controlled to follow the object, whose controller is $\boldsymbol{f}_R = c_v(\boldsymbol{v} - \boldsymbol{v}_R) + c_r(\boldsymbol{r} - \boldsymbol{r}_R)$ where $c_v = 30kg/s$ and $c_r = 20kg/s^2$.

In the simulation, we present several configurations, parts of which are outlined in Table 3. FCDS is employed in the first and second configurations. A validated detumbling strategy proposed by Wallsgrove [33] is used as a benchmark in the third configuration. The benchmark, named as the smooth attitude-stabilizing control (SASC) is similar to the FCDS, except that (50) is replaced by

$$\boldsymbol{u}^i = -u_{\max} \text{Tanh}\left(\frac{\tilde{\boldsymbol{g}}^{i-1}}{u_{\max}}\right) \tag{62}$$

To compare the performance of our estimator on estimating inertia parameter with an existing method in [9], configuration 4 is set.

TABLE 2. Initial values of states/guesses.

Variable	Value	Unit
$\boldsymbol{q}_0$	$[0,0,0,1]^T$	/
$\boldsymbol{q}_{R,0}$	$[0,0,0,1]^T$	/
$\boldsymbol{r}_0$	$[0,0,0]^T$	m
$\boldsymbol{r}_{R,0}$	$[5,0,0]^T$	m
$\boldsymbol{\omega}_0$	$[0.2,0.14,0.15]^T$	rad/s
$\boldsymbol{\omega}_{R,0}$	$[0,0,0]^T$	rad/s
$\boldsymbol{v}_0$	$[0.1,0.05,0.09]^T$	m/s
$\boldsymbol{v}_{R,0}$	$[0,0,0]^T$	m/s
${}^R\boldsymbol{a}_R$	$[0,0,1]^T$	m
$\boldsymbol{l}_{S,0}$	$[320,126,270]^T$	$\text{kg} \cdot \text{m}^2/\text{s}$
${}^U\boldsymbol{\rho}_F$	$[0,0,1]^T$	m
$\boldsymbol{\mu}$	$[0.5,0.5,0.5,0.5]^T$	/
$\hat{\boldsymbol{q}}_0$	$[0.3,0.3,0.3,0.85]^T$	/
$\hat{\boldsymbol{r}}_0$	$[0.5,0.5,0.5]^T$	m
$\hat{\boldsymbol{l}}_{S,0}$	$[320,272,240]^T$	$\text{kg} \cdot \text{m}^2/\text{s}$
$\hat{\boldsymbol{p}}_{S,0}$	$[423,345,207]^T$	$\text{kg} \cdot \text{m/s}$
$\hat{i}_{xx,0}$	1300	$\text{kg} \cdot \text{m}^2$
$\hat{m}_0$	1600	kg
$\hat{\boldsymbol{i}}_{yz,0}$	$[0.8,0.8]^T$	/
$\boldsymbol{p}_{S,0}$	$[120,60,108]^T$	$\text{kg} \cdot \text{m/s}$

TABLE 3. Differences among four configurations.

Configuration	$f_{\max}$	Estimation method	Detumbling strategy
1	200 N	Ours	FCDS
2	123 N	Ours	FCDS
3	200 N	Ours	SASC
4	200 N	Method in [9]	FCDS

The effectiveness of the MCB-SRUKF and the FCDS with configuration 1 is examined in Subsection IV-B. A test on the estimation accuracy of the MCB-SRUKF under different conditions and the comparison between this filter and the benchmark estimator are given in Subsection IV-C. Two detumbling controller, i.e., FCDS and SASC, are compared in Subsection IV-D.

B. TEST 1: SIMULATION RESULTS OF CONFIGURATION 1

The performance of the tracking filter with configuration 1 is examined. In Fig. 6, real and estimated values of all states and intermediate variables are recorded. $\boldsymbol{q}$, $\boldsymbol{r}$, $\boldsymbol{l_S}$, $\boldsymbol{p_S}$, $\boldsymbol{I_{yz}}$, absolute inertia parameters (i_{xx} and m), $\boldsymbol{\omega}$, and $\boldsymbol{v}$ are depicted separately in different subgraphs. Lines of different components are moved downward to different distances so that components of variables can be shown. For example, $\boldsymbol{q} = 0$, $\boldsymbol{q} = -3$, $\boldsymbol{q} = -6$, and $\boldsymbol{q} = -9$ in subgraph (a) are regarded as zero lines of q_1, q_2, q_3, and q_4, which are marked

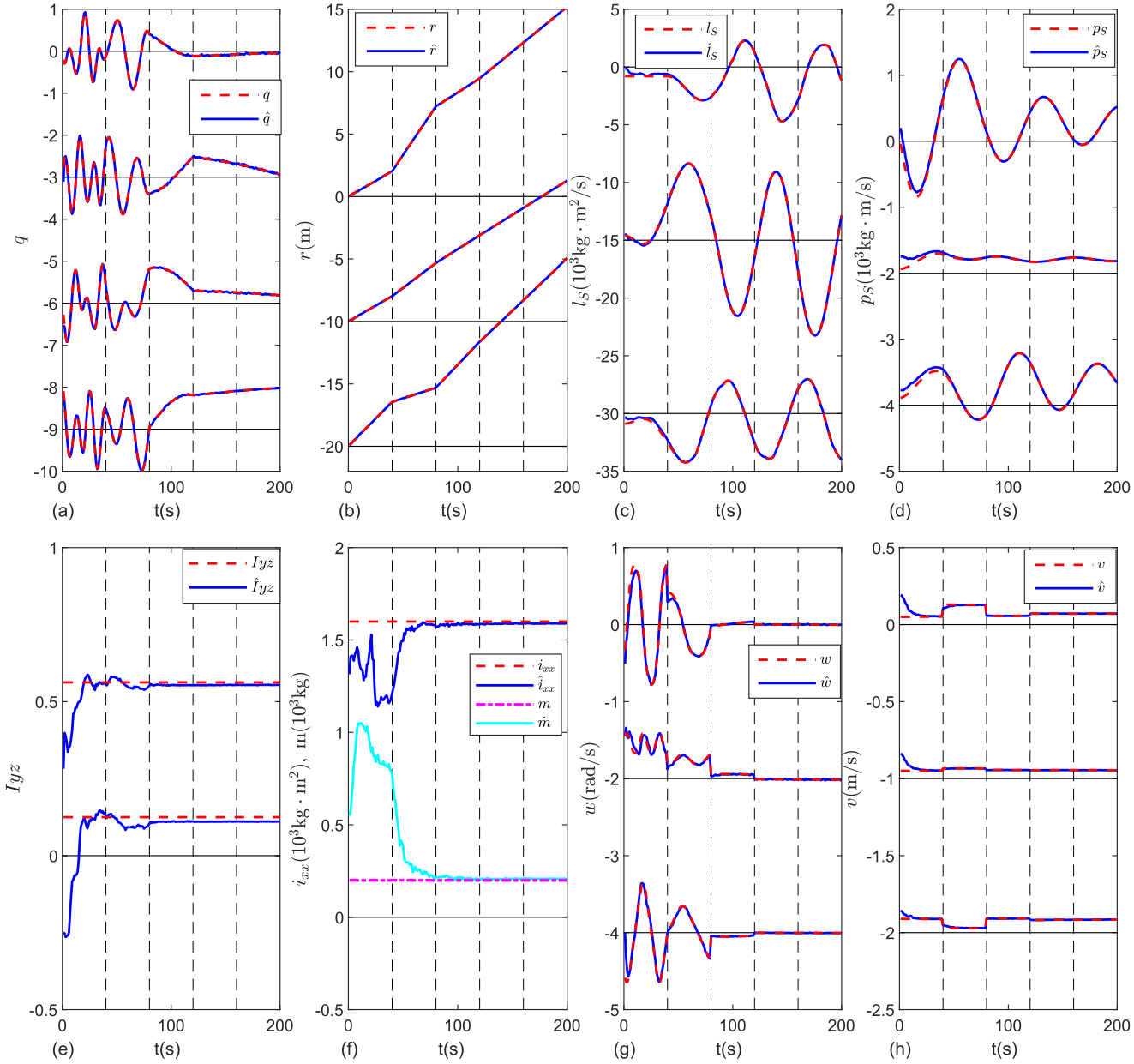

FIGURE 6. Estimation results of the MCB-SRUKF in configuration 1.

with black horizontal lines. In Fig. 6, red dotted curves, blue solid curves, and black dotted vertical lines represent actual values of variables, estimates of variables, and contact events, respectively. In each of subgraphs, there are four black vertical lines, which indicates that the robot touches the object four times. As compared to Fig. 6, Fig. 7 displays errors of variables more clearly. The same translation operation of Fig. 6 is applied to lines of Fig. 7. In this figure, blue solid curves and black dotted curves represent estimation errors and 3σ of variables, respectively. It should be noted that $\boldsymbol{\omega}$ and $\boldsymbol{v}$ are intermediate variables. Therefore, there is no 3σ in Fig. 7 (g) and 7 (h).

As depicted in Fig. 6, the slope of curves of $\boldsymbol{q}$, $\boldsymbol{r}$, $\boldsymbol{\omega}$, and $\boldsymbol{v}$ changes each time the robot touches the object. In contrast to these variables, curves of $\boldsymbol{l_S}$ and $\boldsymbol{p_S}$ are smooth at the moment of contacts. The cause of this phenomenon lies in the momentum conservation law. Fig. 7 (a), 7 (b), 7 (g), and 7 (h) indicate that errors of $\boldsymbol{q}$, $\boldsymbol{r}$, $\boldsymbol{I}_{yz}$, $\boldsymbol{\omega}$, and $\boldsymbol{v}$ converge to zero lines before 40s. $\boldsymbol{\omega}$ and $\boldsymbol{v}$ relate to the translation and rotation motion, respectively. From Fig. 7 (g) and 7 (h), we can see that the filter performs better on a translational motion than a rotational motion. The comparison between $\boldsymbol{l_S}$ and $\boldsymbol{p_S}$ confirms this conclusion. According to Fig. 7 (f), absolute inertia parameters, i.e., i_{xx} and m, cannot be

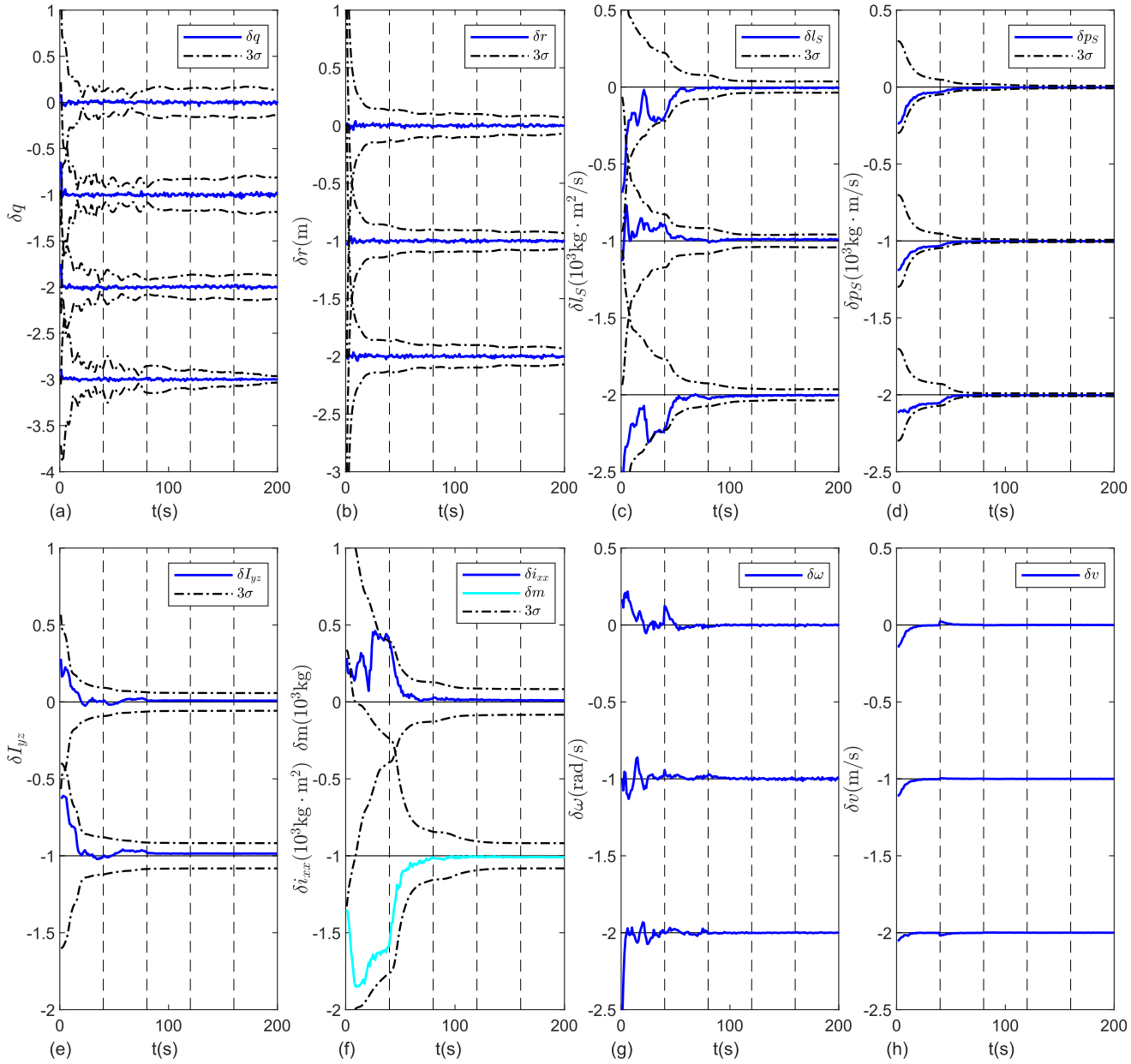

FIGURE 7. Estimation errors of the MCB-SRUKF in configuration 1.

determined before the robot touches the object. (An unlisted test demonstrates that without the influence of the external disturbance, estimated values and 3σ of i_{xx} and m are constant before 40s. Another non-contact research shows that using the external disturbance to estimate inertia parameter is time-consuming and inaccuracy. Therefore, we can conclude that the disturbance is beneficial but insufficient to estimate absolute inertia parameters of the object.) The uncertainties and errors associated with i_{xx} and m rapidly decrease when the contact event occurs. Curves converge to zero in a short period of time following the first contact. Curves of $\boldsymbol{l_S}$ and $\boldsymbol{p_S}$ in Fig. 7 (c) and 7 (d) can be precisely estimated after 40s, which is similar to i_{xx} and m. Therefore, the MCB-SRUKF is confirmed to be semi-activated before 40s and to be fully activated by the first contact. The semi-activated filter is demonstrated to be capable of estimating $\boldsymbol{q}$, $\boldsymbol{r}$, $\boldsymbol{\omega}$, and $\boldsymbol{v}$. The activated filter is proved to be able to estimate all states reliably. In Fig. 7, all estimation curves are within bounds of 3σ. Therefore, the stability and effectiveness of the MCB-SRUKF are verified.

Fig. 7 (g) shows that the object is tumbling at a high speed before the first contact. The output data of the FCDS at all contact events is summarized in Table 4 where ξ_g represents the deviation ratio of the output of the FCDS and can be used

TABLE 4. Outputs of the FCDS. The red number is above normal values.

Variable	1st Contact	2nd Contact	3rd Contact	4th Contact
$c_f(N)$	195.24	199.77	33.50	1.30
$\|\tilde{\boldsymbol{g}}\|\ (N\cdot m)$	597.71	587.31	100.53	3.89
ξ_g	1.17	0.51	**5.11**	**84.76**
$\boldsymbol{\rho_E}$	$\begin{bmatrix}-0.25\\-2.73\\-1.21\end{bmatrix}$	$\begin{bmatrix}0.41\\2.81\\0.97\end{bmatrix}$	$\begin{bmatrix}-0.77\\-2.72\\-0.99\end{bmatrix}$	$\begin{bmatrix}-1.86\\-1.70\\-1.62\end{bmatrix}$

to describe the influence of estimation errors on the FCDS. ξ_g is computed by

$$\xi_g = \frac{\|\boldsymbol{g} - \tilde{\boldsymbol{g}}\|}{\|\tilde{\boldsymbol{g}}\|} \times 100\% \tag{63}$$

The table illustrates that the interaction force at the first and the second contacts is close to the threshold value, i.e., 200N. After the 80s, the angular velocity of the object decreases around zero lines as depicted in Fig. 6 (g). The attitude quaternion correspondingly changes slowly as shown in Fig. 6 (a) After the third contact, the object is detumbled. We can find that differences between ideal detumbling moments and output moments of the FCDS at first two contacts are within a reasonable range. Based on the fact that δi_{xx} and δm are large and that $\tilde{\boldsymbol{g}}$ has a low bias at the first contact, we can conclude that the semi-activated filter almost has no effect on the FCDS. Immediately following the second contact, the ratio increases sharply due to a decreasing magnitude of $\|\tilde{\boldsymbol{g}}\|$. The angular velocity of the object remains near zero despite the disturbance of errors. Therefore, the effectiveness and robustness of the FCDS are verified. (A needless contact, i.e., the fourth contact, is exerted on the object in the simulation even after it has almost stopped rotating. The goal is to test the stability of the FCDS. In practice, the robot can stop the FCDS after completing the third contact or when the angular velocity is sufficiently small.)

C. TEST 2: THE STEADY-STATE ERROR OF THE MCB-SRUKF UNDER DIFFERENT CONDITIONS

The MCB-SRUKF with different configurations is tested in this study case. The simulation is run for 20 times to eliminate the effect of outliers on the steady-state error. The mean absolute error after 80s, denoted by ς^p, is computed considering that all states are estimated stably after the second contact. Take the attitude quaternion as an example. ς^p which corresponds to $\boldsymbol{q}$ can be calculated by using

$$\varsigma^p = \mathrm{E}(\left\|\delta \boldsymbol{q}^p\right\|) \tag{64}$$

where p is the configuration number. A comparison of the ratio of ς^p with different configurations is provided in Table 5 to determine influencing factors of steady-state errors. If the ratio is 1, the performance of the filter with configuration 2 or 3 is similar to the performance of the filter with configuration 1. In the first column of Table 5, ratios corresponding to i_{xx} and m exceed the normal range. Results in the second column are close to 1. Therefore, the magnitude of the interaction force can significantly affect the estimation precision of absolute inertia parameters.

TABLE 5. Estimation errors of three tests. Red numbers are much greater than 1.

Variable	ς^2/ς^1	ς^3/ς^1
$\boldsymbol{q}$	0.9783	0.9879
$\boldsymbol{r}$	1.0396	0.9642
$\boldsymbol{l_S}$	1.8565	1.1498
$\boldsymbol{p_S}$	1.7036	1.0764
$\boldsymbol{I_{yz}}$	0.9596	0.9541
i_{xx}	**8.3580**	1.0772
m	**9.4523**	1.0611
$\boldsymbol{\omega}$	1.2206	0.9342
$\boldsymbol{v}$	1.3783	1.2079

TABLE 6. c_f(N) of three configurations. The magnitude of the contact force which corresponds to the red number is less than others.

Configuration	1st Contact	2nd Contact	3rd Contact	4th Contact
1	199.24	195.77	33.50	**1.30**
2	122.92	122.91	122.49	53.18
3	154.31	126.71	76.27	40.68

To further examine the influence of the interaction force, errors of i_{xx} and m are shown in Fig. 8. The estimation result of i_{xx} in configuration 4 is given in Fig. 8 (a). The estimation on mass of the object is not considered in [9]. Therefore, only configuration 1, 2, and 3 are compared in 8 (b). The first subgraph illustrates that δi_{xx} curves in configuration 1 and 3 are similar. They have fast convergence speeds at the time of the fist contact and can converge before the second contact. In the same period, δi_{xx} curve of the configuration 2 decrease but are not equal to zero. It is only after the third contact that the filter with the configuration 2 is capable of estimating i_{xx} precisely. The same phenomenon of Fig. 8 (a) can be observed in Fig. 8 (b) in regard to configuration 1, 2, and 3. Therefore, the limit of the interaction force, i.e., $f_{\max}$, is the dominant factor affecting the estimation accuracy of inertia parameters. More contacts are required as $f_{\max}$ decreases to ensure a certain level of the estimation accuracy. Different detumbling strategies with the same $f_{\max}$ have little influence on the performance of our estimator. Fig. 8 (a) illustrates that after three contacts, inertia estimator presented in [9] can have a similar precision as our estimator in configuration 1. The benchmark algorithm only samples quantities of velocity every one contacts to compute inertial properties, compared with our work which samples throughout the estimation task. The performance of the benchmark is restricted by inadequate samples. Neglect of the environmental disturbance also reduced its accuracy. Therefore, these factors yield performance disadvantages over our method.

D. TEST 3: THE COMPARISON OF DETUMBLING STRATEGIES

Outputs of the interaction force in configuration 1, 2, and 3 are presented in Table 6. As mentioned before, the object is considered to be detumbled after three contacts

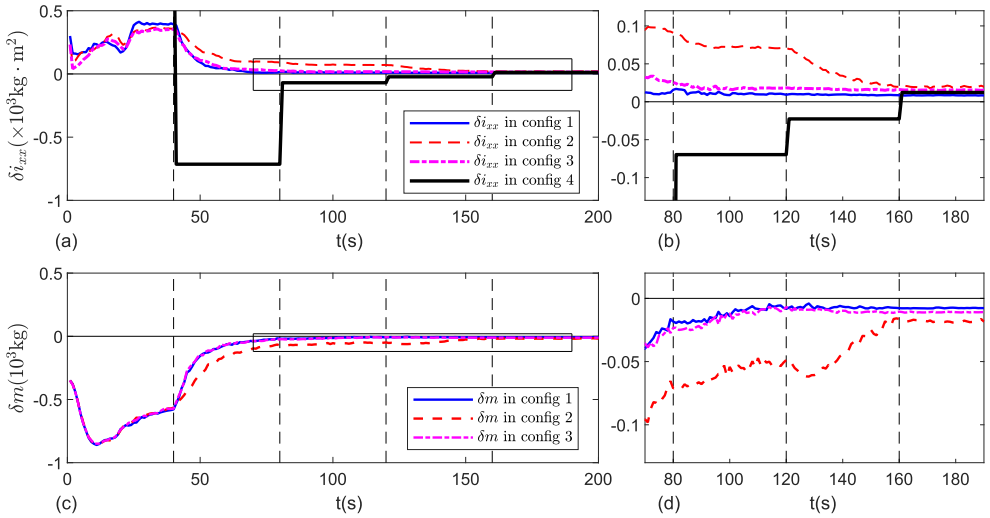

FIGURE 8. Errors of absolute inertia parameters of the filter with different configurations. Rectangular regions of Subgraphs (a) and (c) are displayed enlarged in Subgraphs (b) and (d), respectively.

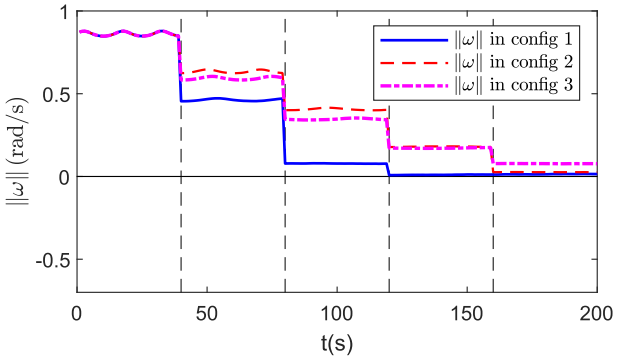

FIGURE 9. The magnitude of residual rotational motion of three configurations.

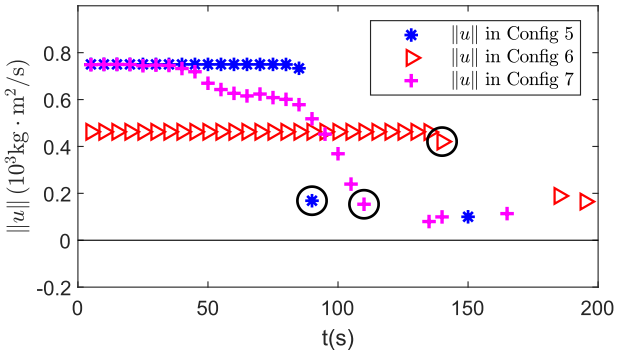

FIGURE 10. The magnitude of u in different configurations. Nominal last contacts are marked by black cycles symbols.

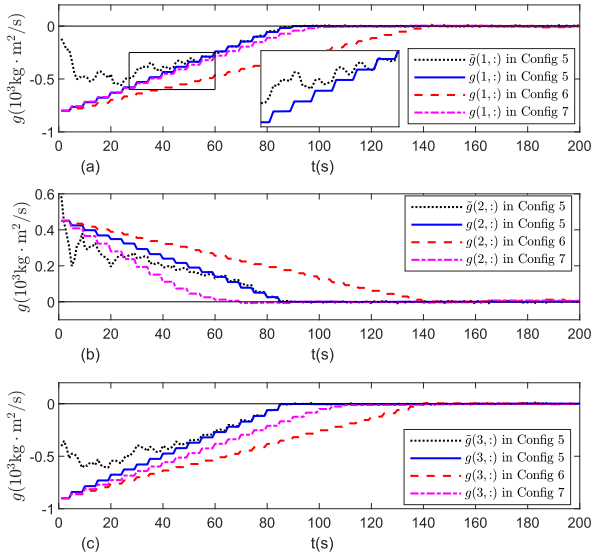

FIGURE 11. Estimated and true values of g in Configuration 5, 6, and 7 are illustrated. Lines of g in three configurations are shown, as well as the curve of $\tilde{g}$ in Configuration 5. $g(i,:)$ represents the set of the i-th component of g. The larger rectangle in (a) illustrates details of g and $\tilde{g}$ in Configuration 5. The object stops tumbling when all components of g converge to zero.

TABLE 7. Differences of three configurations.

Configuration	$f_{\max}$	Detumbling strategy
5	25.0 N	FCDS
6	15.4 N	FCDS
7	25.0 N	SASC

with configuration 1. The table and Fig. 9 illustrate that four contacts are required in configurations 1 and 3 to detumble the object.

To further investigate the performance of difference detumbling strategy, more configurations are given as shown in Table 7. The duration between two contacts is set as 5s. Differ from configuration 1 which keeps detumbling even when the object almost stopped rotating, the robot in configuration 5, 6, and 7 stops the task if $\|\boldsymbol{\omega}\| < 1e{-}2$. The contact of configuration 5 which satisfies the stop condition is marked as a blue star with a black cycle in Fig. 10 and is named as

the nominal last contact. The nominal last contact is a key indicator to evaluate the efficiency of the detumbling strategy. Affected by the measurement disturbance, $\|\hat{\boldsymbol{\omega}}\|$ could exceed 1e-2, which induces the robot to restart the detumbling task. The additional contact of configuration 5 at 150s is caused by this phenomenon and can be ignored. Nominal last contacts of configuration 6 and 7 are also marked in Fig. 10. Therefore, we can conclude that configuration 5, 6, and 7 cost 90s, 140s, and 110s to detumble the object, respectively.

In Fig. 11 (a), $\tilde{\boldsymbol{g}}$ is consistent with $\boldsymbol{g}$ after about 50s. Although $\boldsymbol{g}$ is not estimated precisely before 50s, $\boldsymbol{g}$ is reduced by FCDS at a constant speed. This indicates that FCDS is robust to the measurement error. We can find that three components of $\tilde{\boldsymbol{g}}$ in Configuration 5 and 6 synchronously converge to zero. Components of Configuration 7 spend 95s, 60s, 110s to converge, respectively. SASC can damp the detumbling motion into a simpler rotation motion. Some space robot which can deal with single-axial rotating targets can benefit from SASC.

Therefore, the FCDS is more effective at detumbling the object by using fewer contacts or smaller $f_{\max}$ than the SASC. The efficiency of the FCDS is confirmed by simulation results.

V. CONCLUSION

The MCB-SRUKF and the FCDS have been developed in this paper for the RCDS mission. By combining several techniques including the vision guidance and the momentum transfer computation as well as the dynamic model based on the MC law, a novel navigation method has been constructed. In the FCDS, the angular impulse has been controlled to be the opposite vector of the angular momentum about the CM of the object. A scheme of sub-optimal contact points and interaction forces has been presented to generate a desired impulse. Theoretically, FCDS has been demonstrated to be robust to estimation errors, even when the filter is semi-activated.

In the simulation, the MCB-SRUKF has been demonstrated to be applicable for both contact and free-floating modes. It has been observed that the precision of the proposed estimator about the absolute value of mass and MI increases with the threshold value of the interaction force. Simulations have shown that the designed estimator is not affected by the detumbling strategies employed. MCB-SRUKF has generated more accurate results than the benchmark estimator. Our results regarding the activation of the estimator given in Subsection II-C have been proven. FCDS has been shown to be more efficient than other detumbling approaches. Targets have been detumbled using MCB-SRUKF and FCDS in various configurations. The coupling scheme of the MCB-SRUKF and FCDS has been demonstrated to be stable even when the filter is semi-activated. Our future work will focus on constructing an experimental platform and demonstrating the performance of the coupling scheme in hardware-in-the-loop simulations.

APPENDIX A
DEFINITIONS OF INERTIA PARAMETERS

$\boldsymbol{I} = diag(i_{xx}, i_{yy}, i_{zz})$ is the MI described in $\{\mathcal{U}\}$. $\boldsymbol{I}_{yz}$ and $\boldsymbol{i}_{yz}$ are

$$\boldsymbol{I}_{yz} = diag(1, i_{yy}/i_{xx}, i_{zz}/i_{xx}) \tag{65}$$

$$\boldsymbol{i}_{yz} = \begin{bmatrix} i_{yy}/i_{xx} & i_{zz}/i_{xx} \end{bmatrix}^T \tag{66}$$

Therefore, $\boldsymbol{I}$ can be rewritten as

$$\boldsymbol{I} = i_{xx}\boldsymbol{I}_{yz} \tag{67}$$

APPENDIX B
SQUARE ROOT UNSCENTED KALMAN FILTER

In the following, qr$\{\cdot\}$, chol$\{\cdot\}$, and cholupdate$\{\cdot\}$ stand for the QR decomposition [34], Cholesky decomposition, and Cholesky factor updating, respectively. Initial values of the state and covariance can be provided as

$$\hat{\boldsymbol{x}_0} = E(\boldsymbol{x_0}) \tag{68}$$

$$\hat{\boldsymbol{S}_0} = \text{chol}\left(E\left[(\boldsymbol{x_0} - \hat{\boldsymbol{x}_0})(\boldsymbol{x_0} - \hat{\boldsymbol{x}_0})^T\right]\right) \tag{69}$$

Weight parameters, w_i^m and w_i^c, are computed by

$$w_0^m = \frac{\iota}{N+\iota} \tag{70}$$

$$w_0^c = \frac{\iota}{N+\iota} + 1 - \zeta^2 + \eta \tag{71}$$

$$w_i^m = w_i^c = \frac{\iota}{2(N+\iota)} \quad i \in \{1, \ldots, 2N\} \tag{72}$$

where

$$\iota = N(\zeta^2 - 1) \tag{73}$$

With a prior estimate $\hat{\boldsymbol{x}}_{k-1}$ and $\hat{\boldsymbol{S}}_{k-1}$, sigma points can be computed using

$$\mathcal{X}_{k-1} = \left[\hat{\boldsymbol{x}}_{k-1}\ \hat{\boldsymbol{x}}_{k-1} + \sqrt{L+\iota}\hat{\boldsymbol{S}}_{k-1}\ \hat{\boldsymbol{x}}_{k-1} - \sqrt{L+\iota}\hat{\boldsymbol{S}}_{k-1}\right] \tag{74}$$

Sigma points are propagated through process equations, which are

$$\mathcal{X}_{k|k-1}^{(i)} = \boldsymbol{f}(\mathcal{X}_{k-1}^{(i)}, \boldsymbol{b}_{k-1})\ i \in \{1, \ldots, 2N\} \tag{75}$$

where $\mathcal{X}^{(i)}$ is the i-th column of the matrix $\mathcal{X}$. The mean and the Cholesky factor can be propagated by

$$\hat{\boldsymbol{x}}_{k|k-1} = \sum_{i=0}^{2N} w_i^m \mathcal{X}_{k|k-1}^{(i)} \tag{76}$$

$$\hat{\boldsymbol{S}}_{k|k-1} = \text{cholupdate}\left\{\hat{\boldsymbol{S}}_k',\ \mathcal{X}_{k|k-1}^{(0)} - \hat{\boldsymbol{x}}_{k|k-1},\ w_0^c\right\} \tag{77}$$

$$\hat{\boldsymbol{S}}_k' = \text{qr}\left\{\left[\sqrt{w_i^c}\left[\mathcal{X}_{k|k-1}^{(i=1:2N)} - \hat{\boldsymbol{x}}_{k|k-1}\right]\ \hat{\boldsymbol{G}}\sqrt{\boldsymbol{Q}}\right]\right\} \tag{78}$$

Measurement-transformed sigma points can be calculated by the observation equation (30), which are

$$\mathcal{Z}_{k|k-1}^{(i)} = \boldsymbol{h}(\mathcal{X}_{k|k-1}^{(i)}, \boldsymbol{b}_k), \quad i \in \{0, \ldots, 2N\} \tag{79}$$

The mean measurement vector, the Cholesky factor of observation-error covariance matrix, and the cross-covariance can be computed by

$$\hat{z}_{k|k-1} = \sum_{i=0}^{2N} w_i^m \mathcal{Z}_{k|k-1}^{(i)} \tag{80}$$

$$\hat{S}_{zz,k} = \text{cholupdate}\left\{\hat{S}'_{zz,k},\ \mathcal{Z}_{k|k-1}^{(0)} - \hat{z}_{k|k-1},\ w_0^c\right\} \tag{81}$$

$$\hat{P}_{xz,k} = \sum_{i=0}^{2N} w_i^c (\mathcal{X}_{k|k-1}^{(i)} - \hat{x}_{k|k-1})(\mathcal{Z}_{k|k-1}^{(i)} - \hat{z}_{k|k-1})^T \tag{82}$$

$$\hat{S}'_{zz,k} = \text{qr}\left\{\left[\sqrt{w_i^c}\left[\mathcal{Z}_{k|k-1}^{(i=1:2N)} - \hat{z}_{k|k-1}\right]\ \sqrt{R}\right]\right\} \tag{83}$$

The Kalman gain matrix is computed by

$$K_k = (\hat{P}_{xz,k}/\hat{S}_{zz,k}^T)/\hat{S}_{zz,k} \tag{84}$$

The posteriori estimated state and the Cholesky factor can be updated by

$$\hat{x}_k = \hat{x}_{k|k-1} + K_k(z_k - \hat{z}_{k|k-1}) \tag{85}$$

$$\hat{S}_k = \text{cholupdate}\left\{\hat{S}_{k|k-1},\ K_k\hat{S}_{zz,k},\ -1\right\} \tag{86}$$

APPENDIX C
DERIVATION OF THE OPTIMAL CONTROLLER

The state equation, constraint condition, boundary conditions and cost function are given in Section III-B. The system Hamiltonian can be constructed as:

$$H(\boldsymbol{\lambda}^i, \boldsymbol{g}^{i-1}, \boldsymbol{u}^i) = \boldsymbol{\lambda}^{i,T}(\boldsymbol{g}^{i-1} + \boldsymbol{u}^i) \tag{87}$$

An augmenting discrete performance index is given as follows:

$$J^a = M + \sum_{i=1}^{M} [H(\boldsymbol{\lambda}^i, \boldsymbol{g}^{i-1}, \boldsymbol{u}^i) - \boldsymbol{\lambda}^{i,T}\boldsymbol{g}^i] \tag{88}$$

where $\boldsymbol{\lambda}$ is the costate vector. According to the optimal control theory, the costate must satisfy

$$\boldsymbol{\lambda}^{i-1,*} = \frac{\partial H(\boldsymbol{\lambda}^{i,*}, \boldsymbol{g}^{i-1,*}, \boldsymbol{u}^{i,*})}{\partial \boldsymbol{g}^{i-1}} = \boldsymbol{\lambda}^{i,*} \tag{89}$$

Therefore, $\boldsymbol{\lambda}^*$ is a constant vector, denoted as $\boldsymbol{\lambda}_0$. Pontryagin's minimum principle indicates that optimal torque $\boldsymbol{u}^*$ satisfies the equation:

$$H(\boldsymbol{\lambda}^{i,*}, \boldsymbol{g}^{i-1,*}, \boldsymbol{u}^{i,*}) \leq H(\boldsymbol{\lambda}^{i,*}, \boldsymbol{g}^{i-1,*}, \boldsymbol{u}^i) \tag{90}$$

where $\boldsymbol{u}^i \in \mathbb{R}^3 \ni \|\boldsymbol{u}^i\| \leq u_{\max}$ for every $i \in [1, M]$. We can solve $\boldsymbol{u}^{i,*}$ as a function of costate:

$$\boldsymbol{u}^{i,*} = -u_{\max}\frac{\boldsymbol{\lambda}_0}{\|\boldsymbol{\lambda}_0\|} \tag{91}$$

$\boldsymbol{u}^{i,*}$ is also invariable. Combing (91) and boundary conditions, i.e., (45) and (46), an equation can be given:

$$\boldsymbol{g}^0 - Mu_{\max}\frac{\boldsymbol{\lambda}_0}{\|\boldsymbol{\lambda}_0\|} = 0 \tag{92}$$

Therefore, the unit vector of $\boldsymbol{g}^0$ is identical that of $\boldsymbol{\lambda}_0$. We can conclude that

$$\boldsymbol{u}^{i,*} = -u_{\max}\frac{\boldsymbol{g}^0}{\|\boldsymbol{g}^0\|} \tag{93}$$

ACKNOWLEDGMENT

The authors would like to thank editors and anonymous reviewers for their comments and constructive suggestions that helped to improve this paper significantly.

REFERENCES

[1] A. Flores-Abad, O. Ma, K. Pham, and S. Ulrich, "A review of space robotics technologies for on-orbit servicing," *Prog. Aerosp. Sci.*, vol. 68, pp. 1–26, Jul. 2014, doi: 10.1016/j.paerosci.2014.03.002.

[2] S. Matunaga, T. Kanzawa, and Y. Ohkami, "Rotational motion-damper for the capture of an uncontrolled floating satellite," *Control Eng. Pract.*, vol. 9, no. 2, pp. 199–205, 2001, doi: 10.1016/s0967-0661(00)00098-8.

[3] S. Kawamoto, K. Matsumoto, and S. Wakabayashi, "Ground experiment of mechanical impulse method for uncontrollable satellite capturing," in *Proc. 6th Int. Symp. Artif. Intell. Robot. Automat. Space (i-SAIRAS)*, 2001, pp. 1–8.

[4] S. Yoshikawa and K. Yamada, "Impulsive control for angular momentum management of tumbling spacecraft," *Acta Astronautica*, vol. 60, nos. 10–11, pp. 810–819, May 2007, doi: 10.1016/j.actaastro.2006.10.012.

[5] U. Hillenbrand and R. Lampariello, "Motion and parameter estimation of a free-floating space object from range data for motion prediction," in *Proc. i-SAIRAS*, 2005, pp. 1–10.

[6] F. Aghili, M. Kuryllo, G. Okouneva, and C. English, "Fault-tolerant position/attitude estimation of free-floating space objects using a laser range sensor," *IEEE Sensors J.*, vol. 11, no. 1, pp. 176–185, Jan. 2011, doi: 10.1109/jsen.2010.2056365.

[7] J. Guo, Y. He, X. Qi, G. Wu, Y. Hu, B. Li, and J. Zhang, "Real-time measurement and estimation of the 3D geometry and motion parameters for spatially unknown moving targets," *Aerosp. Sci. Technol.*, vol. 97, Feb. 2020, Art. no. 105619.

[8] C. Ma, H. Dai, C. Wei, and J. Yuan, "Two-stage filter for inertia characteristics estimation of high-speed tumbling targets," *Aerosp. Sci. Technol.*, vol. 89, pp. 333–344, Jun. 2019.

[9] M. Chuan and J. Jianping, "Inertia estimation of tumbling space debris via tentative contacts before capturing," in *Proc. Int. Astron. Congr. (IAC)*, Bremen, Germany, vol. 2018, Oct. 2018.

[10] Q. Meng, J. Liang, and O. Ma, "Identification of all the inertial parameters of a non-cooperative object in orbit," *Aerosp. Sci. Technol.*, vol. 91, pp. 571–582, Aug. 2019, doi: 10.1016/j.ast.2019.05.047.

[11] Y. Murotsu, K. Senda, M. Ozaki, and S. Tsujio, "Parameter identification of unknown object handled by free-flying space robot," *J. Guid., Control, Dyn.*, vol. 17, no. 3, pp. 488–494, May 1994, doi: 10.2514/3.21225.

[12] S. Abiko and G. Hirzinger, "On-line parameter adaptation for a momentum control in the post-grasping of a tumbling target with model uncertainty," in *Proc. IEEE/RSJ Int. Conf. Intell. Robots Syst.*, Oct. 2007, pp. 847–852, doi: 10.1109/iros.2007.4399190.

[13] W. Chu, S. Wu, Z. Wu, and Y. Wang, "Least square based ensemble deep learning for inertia tensor identification of combined spacecraft," *Aerosp. Sci. Technol.*, vol. 106, Nov. 2020, Art. no. 106189.

[14] F. Aghili and K. Parsa, "Motion and parameter estimation of space objects using laser-vision data," *J. Guid., Control, Dyn.*, vol. 32, no. 2, pp. 538–550, Mar. 2009, doi: 10.2514/1.37129.

[15] F. Aghili and C.-Y. Su, "Robust relative navigation by integration of ICP and adaptive Kalman filter using laser scanner and IMU," *IEEE/ASME Trans. Mechatronics*, vol. 21, no. 4, pp. 2015–2026, Aug. 2016, doi: 10.1109/TMECH.2016.2547905.

[16] F. Aghili, "Pre- and post-grasping robot motion planning to capture and stabilize a tumbling/drifting free-floater with uncertain dynamics," in *Proc. IEEE Int. Conf. Robot. Autom.*, May 2013, pp. 5461–5468, doi: 10.1109/icra.2013.6631360.

[17] D. Sheinfeld and S. Rock, "Rigid body inertia estimation with applications to the capture of a tumbling satellite," in *Proc. 19th AAS/AIAA Spaceflight Mech. Meeting*, vol. 134, 2009, pp. 343–356.

[18] Z. Chu, Y. Ma, Y. Hou, and F. Wang, "Inertial parameter identification using contact force information for an unknown object captured by a space manipulator," *Acta Astronautica*, vol. 131, pp. 69–82, Feb. 2017, doi: 10.1016/j.actaastro.2016.11.019.
[19] L. Zong, J. Luo, M. Wang, and J. Yuan, "Parameters concurrent learning and reactionless control in post-capture of unknown targets by space manipulators," *Nonlinear Dyn.*, vol. 96, no. 1, pp. 443–457, Apr. 2019, doi: 10.1007/s11071-019-04798-w.
[20] L. Li, J. Zhang, S. Zhao, R. Qi, and Y. Li, "Autonomous onboard estimation of mean orbital elements for geostationary electric-propulsion satellites," *Aerosp. Sci. Technol.*, vol. 94, Nov. 2019, Art. no. 105369.
[21] F. Aghili, "A prediction and motion-planning scheme for visually guided robotic capturing of free-floating tumbling objects with uncertain dynamics," *IEEE Trans. Robot.*, vol. 28, no. 3, pp. 634–649, Jun. 2012, doi: 10.1109/tro.2011.2179581.
[22] J. Liang and O. Ma, "Angular velocity tracking for satellite rendezvous and docking," *Acta Astronautica*, vol. 69, nos. 11–12, pp. 1019–1028, Dec. 2011, doi: 10.1016/j.actaastro.2011.07.009.
[23] O. Ma, A. Flores-Abad, and T. Boge, "Use of industrial robots for hardware-in-the-loop simulation of satellite rendezvous and docking," *Acta Astron.*, vol. 81, no. 1, pp. 335–347, 2012, doi: 10.1016/j.actaastro.2012.08.003.
[24] G. Dong and Z. H. Zhu, "Autonomous robotic capture of non-cooperative target by adaptive extended Kalman filter based visual servo," *Acta Astronautica*, vol. 122, pp. 209–218, May 2016, doi: 10.1016/j.actaastro.2016.02.003.
[25] B. Naveen, S. V. Shah, and A. K. Misra, "Momentum model-based minimal parameter identification of a space robot," *J. Guid., Control, Dyn.*, vol. 42, no. 3, pp. 508–523, Mar. 2019, doi: 10.2514/1.g003541.
[26] F. James, S. Shah, A. Singh, K. Krishna, and A. Misra, "Reactionless maneuvering of a space robot in precapture phase," *J. Guid., Control Dyn.*, vol. 39, no. 10, pp. 2419–2425, 2016, doi: 10.2514/1.g001828.
[27] M. E. Pittelkau, "Kalman filtering for spacecraft system alignment calibration," *J. Guid., Control, Dyn.*, vol. 24, no. 6, pp. 1187–1195, 2012, doi: 10.2514/3.22615.
[28] D. Che, Z. Zheng, and J. Yuan, "An innovate filter for space robots to unfirmly capture tumbling targets," *Int. J. Adapt. Control Signal Process.*, vol. 36, no. 2, pp. 282–299, Jun. 2021.
[29] C. Ma, C. Wei, and J. Yuan, "Semisynchronizing strategy for capturing a high-speed tumbling target," *J. Guid., Control, Dyn.*, vol. 41, no. 12, pp. 2615–2632, Dec. 2018, doi: 10.2514/1.G003459.
[30] S. Wu, F. Mou, Q. Liu, and J. Cheng, "Contact dynamics and control of a space robot capturing a tumbling object," *Acta Astronaut.*, vol. 151, pp. 532–542, Oct. 2018, doi: 10.1016/j.actaastro.2018.06.052.
[31] F. Aghili, "Time-optimal detumbling control of spacecraft," *J. Guid., Control, Dyn.*, vol. 32, no. 5, pp. 1671–1675, Sep. 2009, doi: 10.2514/1.43189.
[32] K. Yoshida, "The SpaceDyn: A MATLAB toolbox for space and mobile robots," *J. Robot. Mechatronics*, vol. 12, no. 4, pp. 411–416, Aug. 2000, doi: 10.20965/jrm.2000.p0411.
[33] R. J. Wallsgrove and M. R. Akella, "Globally stabilizing saturated attitude control in the presence of bounded unknown disturbances," *J. Guid., Control, Dyn.*, vol. 28, no. 5, pp. 957–963, Sep./Oct. 2005, doi: 10.2514/1.9980.
[34] R. Van der Merwe and E. Wan, "The square-root unscented Kalman filter for state and parameter-estimation," in *Proc. IEEE Int. Conf. Acoust., Speech, Signal Process.*, vol. 6, May 2001, pp. 3461–3464, doi: 10.1109/ICASSP.2001.940586.

DEJIA CHE is currently pursuing the Ph.D. degree with the School of Astronautics, Northwestern Polytechnical University, Xi'an, Shaanxi, China. His research interests include on-orbit service, data fusion, and machine vision.

ZIXUAN ZHENG received the Ph.D. degree in aerospace engineering from the Delft University of Technology. He has been an Assistant Professor with the School of Astronautics, Northwestern Polytechnical University. His research interests include the autonomous planning for multi-agent systems and on-on-orbit service.

JIANPING YUAN received the Ph.D. degree in flight dynamics from Northwestern Polytechnical University. He is currently working as a Professor with Northwestern Polytechnical University. His research interests include on-orbit service, intelligent control, and game theory.